

# Improvement of Transparent Conducting Performance on Oxygen-Activated Fluorine-Doped Tin Oxide Electrodes Formed by Horizontal Ultrasonic Spray Pyrolysis Deposition

Bon-Ryul Koo,<sup>†</sup> Dong-Hyeun Oh,<sup>‡</sup> Doh-Hyung Riu,<sup>\*,‡,§</sup> and Hyo-Jin Ahn<sup>\*,†,‡,§</sup>

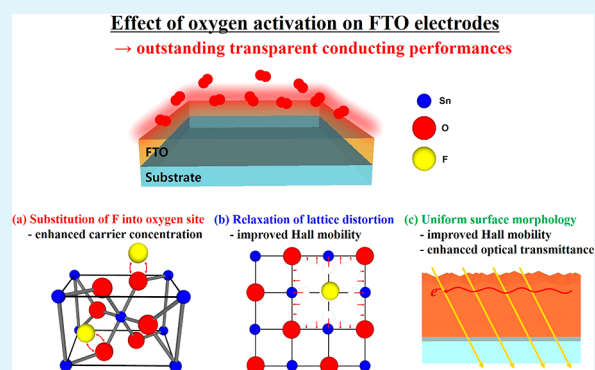
<sup>†</sup>Program of Materials Science & Engineering, Convergence Institute of Biomedical Engineering and Biomaterials and <sup>‡</sup>Department of Materials Science and Engineering, Seoul National University of Science and Technology, Seoul 01811, Korea

<sup>§</sup>Research Institute for FTO, ceon Co., Ltd., Suwon-si, Gyeonggi-do 16642, Korea

## Supporting Information

**ABSTRACT:** In this study, highly transparent conducting fluorine-doped tin oxide (FTO) electrodes were fabricated using the horizontal ultrasonic spray pyrolysis deposition. In order to improve their transparent conducting performances, we carried out oxygen activation by adjusting the ratio of O<sub>2</sub>/(O<sub>2</sub>+N<sub>2</sub>) in the carrier gas (0%, 20%, and 50%) used during the deposition process. The oxygen activation on the FTO electrodes accelerated the substitution concentration of F (F<sub>O</sub><sup>•</sup>) into the oxygen sites in the FTO electrode while the oxygen vacancy (V<sub>O</sub><sup>••</sup>) concentration was reduced. In addition, due to growth of pyramid-shaped crystallites with (200) preferred orientations, this oxygen activation caused the formation of a uniform surface structure. As a result, compared to others, the FTO electrode prepared at 50% O<sub>2</sub> showed excellent electrical and optical properties (sheet resistance of  $\sim 4.0 \pm 0.14 \Omega/\square$ , optical transmittance of  $\sim 85.3\%$ , and figure of merit of  $\sim 5.09 \pm 0.19 \times 10^{-2} \Omega^{-1}$ ). This led to a superb photoconversion efficiency ( $\sim 7.03 \pm 0.20\%$ ) as a result of the improved short-circuit current density. The photovoltaic performance improvement can be defined by the decreased sheet resistance of FTO used as a transparent conducting electrode in dye-sensitized solar cells (DSSCs), which is due to the combined effect of the high carrier concentration by the improved F<sub>O</sub><sup>•</sup> concentration on the FTO electrodes and the fasted Hall mobility by the formation of a uniform FTO surface structure and distortion relaxation on the FTO lattices resulting from the reduced V<sub>O</sub><sup>••</sup> concentration.

**KEYWORDS:** transparent conducting electrode, fluorine-doped tin oxide, oxygen activation, film structures, horizontal ultrasonic spray pyrolysis deposition, photovoltaic performance



## INTRODUCTION

Due to their numerous advantages, such as a simple device structure, cost-effective fabrication, flexibility, and various applications, dye-sensitized solar cells (DSSCs), based on the principle of photosynthesis, have been widely known as a potential alternative to conventional silicon-based solar cells.<sup>1–3</sup> These factors are what makes DSSCs attractive for solar cell fields requiring large scale process, flexibility, and environmentally friendly elements.<sup>4</sup> Typical DSSCs are composed of transparent conducting electrodes (TCEs), nanosized TiO<sub>2</sub> working electrodes, sensitizing dyes, Pt counter electrodes, and iodide electrolyte.<sup>5</sup> Over the last several years, considerable effort had been invested into seeking to enhance the photoconversion efficiency of DSSCs in terms of development of porous working electrodes, effective light-absorbing dyes, and low-cost counter electrodes.<sup>6–8</sup> However, although the TCE is one of the essential components in DSSCs, relevant research on high-performance TCEs for improving their photovoltaic properties is scarce.<sup>9–13</sup>

In general, due to their low resistivity ( $<10^{-4} \Omega \text{ cm}$ ) and high optical transparency ( $>80\%$ ) in the visible region, the TCEs have long been used in a great variety of optoelectronic applications, such as touch screens, smart windows, liquid crystal displays (LCD), organic light emitting diode displays, and solar cells. Up to now, as most extensively investigated TCE materials, there are doped metal oxides with a wide band gap ( $>3 \text{ eV}$ ), such as tin-doped indium oxide (ITO), aluminum-doped zinc oxide (AZO), and fluorine-doped tin oxide (FTO). In particular, the FTO was the most widely used TCE for DSSCs due to its good stabilities in acid atmosphere and at high temperature.<sup>14,15</sup> In DSSCs, the FTO plays an important part that determines the amount of light entering the device and transfers the photoelectrons to the external circuit, which is directly related to the photovoltaic performances of

Received: August 28, 2017

Accepted: December 1, 2017

Published: December 1, 2017

DSSCs.<sup>15,16</sup> More specifically, sheet resistance and optical transparency in the FTO electrodes that are critical factors to determine the photovoltaic performances largely depend on their defect structures (substitution of F on oxygen site ( $F_{O^{\bullet}}$ ) and oxygen vacancy ( $V_{O^{\bullet\bullet}}$ )) and crystallographic structures (crystallinity, grain, and morphology).<sup>15–18</sup> Therefore, many previous studies have been sought to adjust these structures for high-performance FTO electrodes through various synthetic methods, including RF magnetron sputtering, chemical vapor deposition, pulsed laser deposition, spin coating, and ultrasonic spray pyrolysis deposition (USPD).<sup>19–23</sup> In particular, the commercial FTO electrodes of Pilkington (TEC8) were fabricated by an atmospheric pressure chemical vapor deposition whereby an inert gas (99.99%) was used to transport metal–organic precursor into the reaction chamber.<sup>24</sup> In addition, Jeon et al. used the electron cyclotron resonance-metal organic chemical vapor deposition method to prepare the high-performance FTO electrodes, whose chemical species are able to deposit on the substrate by high-impact energy induced from plasma bombardment at the optimum base and working pressures of  $\sim 2 \times 10^{-6}$  and  $\sim 1 \times 10^{-3}$  Torr, respectively.<sup>25</sup>

Normal USPD is a simple and cost-effective synthetic method to fabricate the film nanostructures using precursor droplets (1–100  $\mu\text{m}$  in size) formed by the ultrasonic atomization.<sup>23</sup> Furthermore, this method can easily vary the FTO properties (e.g., textures, morphologies, substitution concentrations, etc.) by adjusting the compositions of the precursor solution (e.g., solvents, additives, and viscosity) and process parameters (e.g., flow rate, ultrasonic amplitude, and deposition temperature).<sup>26–28</sup> For example, Agashe et al. reported the thickness effect of spray pyrolyzed FTO electrodes on the TCE performances and the FTO electrodes with 1000 nm thickness possessing the minimum resistivity of  $\sim 3 \times 10^{-4} \Omega \text{ cm}$  and a good visible transmittance of  $\sim 84\%$ .<sup>26</sup> Furthermore, Benhaoua et al. controlled the fluorine concentration on the FTO electrodes and revealed the optimized TCE performances with minimum resistivity ( $\sim 1.4 \times 10^{-3} \Omega \text{ cm}$ ) and maximum transmittance ( $\sim 83.9\%$ ) at 4 wt % F.<sup>27</sup> Likewise, Otsuka et al. reported the surface modification of spray pyrolyzed FTO electrodes using ITO nanoparticle seed layers, which effectively enhanced their haze values to enhance the light harvest with the scattering.<sup>28</sup> However, while these developments can contribute to the improvement of photovoltaic performance in the DSSC, the conventional USPD technique limits the precise investigation of the effect of chemical and oxygen potential for the FTO electrodes, because its deposition chamber is an open system exposed to the air atmosphere by ca. 20%.<sup>26–28</sup> Hence, the study of oxygen activation on the FTO electrodes using USPD has not been reported yet. In addition, from this standpoint, the efforts to investigate the relationship between the FTO electrode and the photovoltaic performance are a very critical issue for DSSC.

In the present study, we fabricated highly transparent conducting FTO electrodes using the horizontal ultrasonic spray pyrolysis deposition (HUSPD, ceon, Nano SPD, TV500, Korea) with a closed atmosphere chamber to ensure a steady semiequilibrium state during the FTO deposition and investigated the effect of oxygen activation on the FTO electrodes by adjusting  $O_2$  ratio in the carrier gas (0%, 20%, and 50%) to enhance their transparent conducting performance. In addition, we studied the relationship between their transparent conducting performance and the photovoltaic performance of DSSCs.

## RESULTS AND DISCUSSION

Figure 1a shows a schematic representation of the HUSPD used for fabricating the FTO electrodes. This apparatus consists

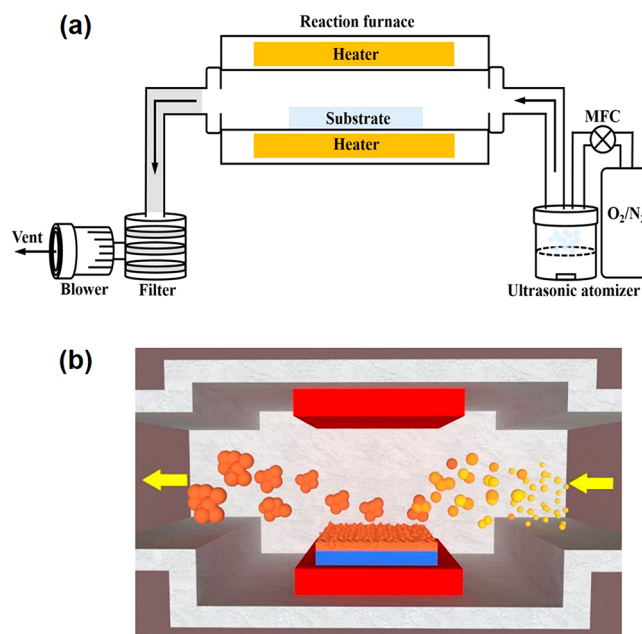


**Figure 1.** Schematic representation of (a) the horizontal ultrasonic spray pyrolysis deposition technique and (b) the deposition process for fabricating the film nanostructure in reaction furnace.

of a mass flow controller, a spraying bath with ultrasonic atomizer, a reaction furnace, and residual particle filter, which is similar to that of the normal USPD. However, for the normal USPD, the spraying head is positioned above the substrate surface and the precursor solution is vertically supplied to the substrate. In this case, the chemical species in the sprayed droplets are agglomerated on the substrates due to nonuniform distribution of gas flow through spray head, which can lead to the formation of nonuniform film nanostructure.<sup>29,30</sup> On the other hand, the HUSPD is allowed to horizontally supply the precursor solution to a reaction furnace. Since it is considered to be the uniform gas flow, the precursor droplets formed by ultrasonic atomizer directly undergo the following uniform formation process for fabricating a film nanostructure in a reaction furnace (see Figure 1b): (1) solvent evaporation, (2) solute condensation, and (3) thermal decomposition (can be generated by the following chemical reactions:  $\text{SnCl}_4 + 2\text{H}_2\text{O} + \text{NH}_4\text{F} \rightarrow \text{SnO}_2\text{:F} + 3\text{HCl} + \text{NH}_4\text{Cl} + \text{HF}$ ).<sup>31</sup> In addition, unlike the normal USPD, it can adjust the deposition atmosphere in the closed chamber during the formation of film nanostructure. Therefore, the HUSPD can result in a successful formation of the high-performance FTO electrodes through oxygen activation.

Figure 2 shows X-ray diffraction patterns of the FTO electrodes formed at varied  $O_2$  ratio in the carrier gas for oxygen activation. All electrodes present a polycrystalline structure with characteristic diffraction peaks at  $26.50^\circ$ ,  $33.84^\circ$ ,  $37.94^\circ$ , and  $51.74^\circ$ , indicating the (110), (101), (200), and (211) planes of a tetragonal rutile  $\text{SnO}_2$  (space group  $P42/mnm$  [136], JCPDS no. 88-0287), respectively. Specifically, a close investigation reveals that these diffraction peaks are slightly shifted to a lower angle than the pure  $\text{SnO}_2$

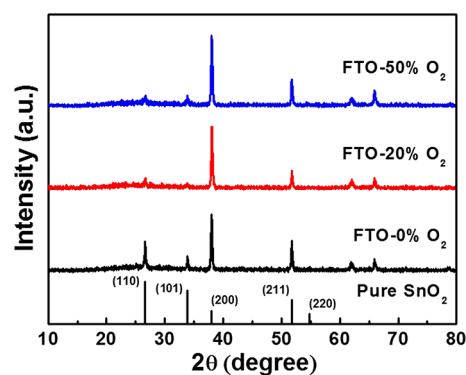


**Figure 2.** X-ray diffraction patterns of the FTO electrodes fabricated using HUSPD at the different  $O_2$  ratio in the carrier gas.

shown at the bottom ( $26.61^\circ$  for (110) plane,  $33.90^\circ$  for (101) plane,  $37.98^\circ$  for (200) plane, and  $51.82^\circ$  for (211) plane). This implies that the FTO phases are successfully formed as the substitution of smaller  $O^{2-}$  (ionic radius 0.132 nm) by a larger  $F^-$  (ionic radius 0.133 nm) in the  $SnO_2$ , which can be defined by Bragg's equation ( $n\lambda = 2d \sin \theta$ ).<sup>32</sup> Interestingly, with an increase of the  $O_2$  ratio in the carrier gas, the intensity ratio between (200) and (110) planes gradually increases (2.5 for FTO-0%  $O_2$ , 11.4 for FTO-20%  $O_2$ , and 14.6 for FTO-50%  $O_2$ ). This particular change can be altered by the growth of the preferred orientation in the  $SnO_2$ .<sup>33,34</sup> According to the periodic bond chain theory, the (110) and (200) preferred orientations of the  $SnO_2$  are formed by (101) F-faces and (111) K-faces, respectively. In the thermodynamic stable condition, it is well-known that the  $SnO_2$  has dominant (110) preferred orientations by the formation of (101) F-faces.<sup>33</sup> However, as shown in previous reports, at high oxygen concentration, the suppression of (101) F-faces by (111) K-faces was accelerated due to the adsorption of polar halogen-rich gases formed as byproducts of tin chloride precursors.<sup>33</sup> Therefore, an increase in the  $O_2$  ratio during the spray pyrolysis can suppress the growth of (110) preferred orientations, leading to the growth of the crystalline  $SnO_2$  phases with dominant (200) preferred orientations. Therefore, this can cause the formation of a uniform surface in the FTO electrodes because the formed

(200) preferred orientations are parallel to the glass substrate, which is an important factor for enhancing the electrical properties of TCEs.<sup>35</sup>

Figure 3 shows the top-view and cross-view FESEM images of (a,d) FTO-0%  $O_2$ , (b,e) FTO-20%  $O_2$ , and (c,f) FTO-50%  $O_2$ , respectively. For the top-view FESEM images, it is observed that the crystallites are well interlocked throughout the entire surface of all of the electrodes. In particular, the morphology and grain size of the crystallites differ among the electrodes. FTO-0%  $O_2$  is composed of the majority of rod-shaped crystallites ( $\sim 423.5$ – $585.9$  nm) and the few pyramid-shaped crystallites ( $\sim 170.9$ – $313.7$  nm) where partial pinholes are observed on the surface due to the different shapes between the crystallites. However, as the  $O_2$  ratio in carrier gas increases, the distribution of the rod-shaped crystallites is gradually reduced. Finally, FTO-50%  $O_2$  display only the pyramid-shaped crystallites of the size in the range of  $\sim 197.8$ – $311.9$  nm, without formation of rod-shaped crystallites. These phenomena are related to the growth suppression of the crystallites induced by a low surface energy at a high  $O_2$  ratio in the carrier gas.<sup>14,36</sup> According to the nucleation theory, the nucleation density ( $N$ ) can be defined as follows (see eq 1):<sup>37</sup>

$$N = A \exp(-\Delta G/RT) \quad (1)$$

where  $\Delta G$  is the activation energy of nucleation corresponding to the surface free energy ( $\Delta G_s$ ) and the volume free energy ( $\Delta G_v$ ).  $A$ ,  $R$ , and  $T$  are a constant, a gas constant, and a growth temperature, respectively. That is, the increase of the  $O_2$  ratio during the deposition process causes a decrease in the surface free energy. Therefore, in FTO-50%  $O_2$ , the growth of (110) planes corresponding to the rod-shaped crystallites is suppressed due to their decreased activation energy of nucleation.<sup>38,39</sup> From cross-view FESEM images shown in Figure 3d–f, the thicknesses of FTO-0%  $O_2$ , FTO-20%  $O_2$ , and FTO-50%  $O_2$  are observed to be  $\sim 491.6$ – $624.2$  nm (ca. 561.1 nm),  $\sim 495.5$ – $619.4$  nm (ca. 557.8 nm), and  $\sim 517.5$ – $621.1$  nm (ca. 558.3 nm), respectively, thus resulting in that their values of  $\Delta$ thickness/thickness were gradually decreased with an increase of the  $O_2$  ratio (23.6% for FTO-0%  $O_2$ , 22.2% for FTO-20%  $O_2$ , and 18.5% for FTO-50%  $O_2$ ). These results implied that an increase of the  $O_2$  ratio can cause the formation

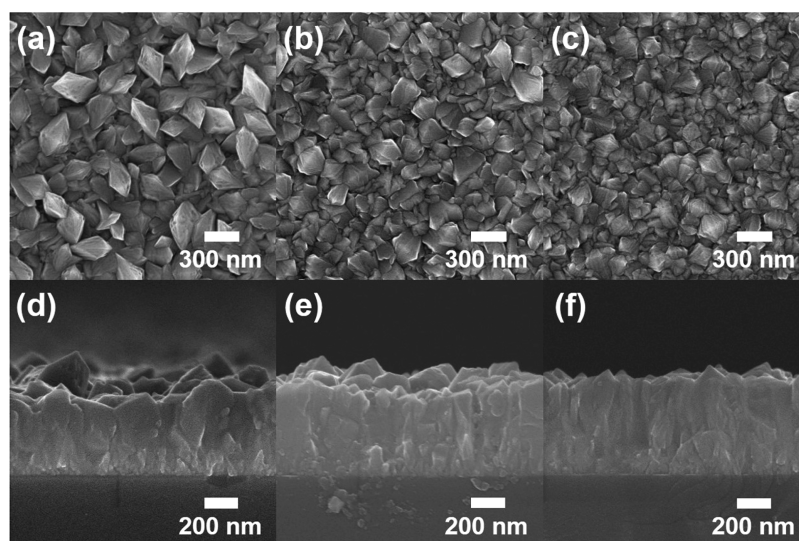


**Figure 3.** (a–c) Top-view FESEM images and (d–f) cross-view FESEM images of FTO-0%  $O_2$ , FTO-20%  $O_2$ , and FTO-50%  $O_2$ , respectively.

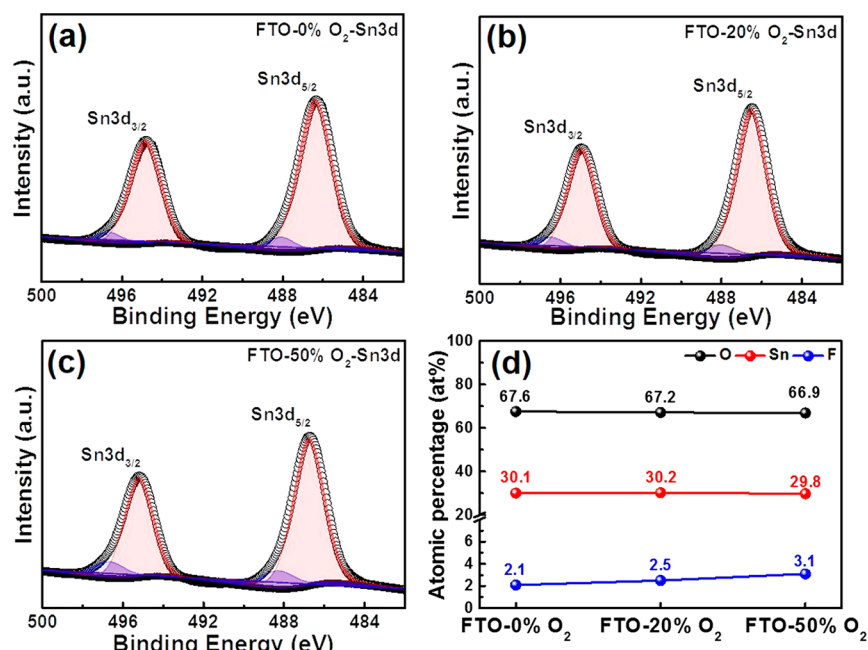


**Figure 4.** XPS core-level spectra of Sn 3d obtained from (a) FTO-0% O<sub>2</sub>, (b) FTO-20% O<sub>2</sub>, and (c) FTO-50% O<sub>2</sub> and (d) atomic percentages of O, Sn, and F elements for all of the electrodes.

of film structure with uniform thickness while there was no a critical difference of average thickness among the samples. Furthermore, for the surface morphology, with an increase of the O<sub>2</sub> ratio in the carrier gas, it changes from a rough surface to a uniform surface due to the growth suppression of the rod-shaped crystallites with apices. This result is convincingly demonstrated by the AFM images in Figure S1. With regard to FTO-0% O<sub>2</sub> (Figure S1a), it should be noted that the majority of the rod-shaped crystallites protruding in the upward direction are irregularly distributed in the FTO surface. However, as the O<sub>2</sub> ratio in the carrier gas increases, the distribution of the rod-shaped crystallites is gradually decreased, which is related to the growth suppression of (110) preferred orientations in the SnO<sub>2</sub> phases observed in the XRD results, leading to a decrease in the root-mean-square roughness ( $R_{\text{ms}}$ ) of the FTO electrode ( $\sim 39.0$  nm for FTO-0% O<sub>2</sub>,  $\sim 31.8$  nm for FTO-20% O<sub>2</sub>, and 29.1 nm for FTO-50% O<sub>2</sub>). Therefore, the SEM and AFM results indicate that, as compared to other electrodes, FTO-50% O<sub>2</sub> possess a uniform surface morphology.

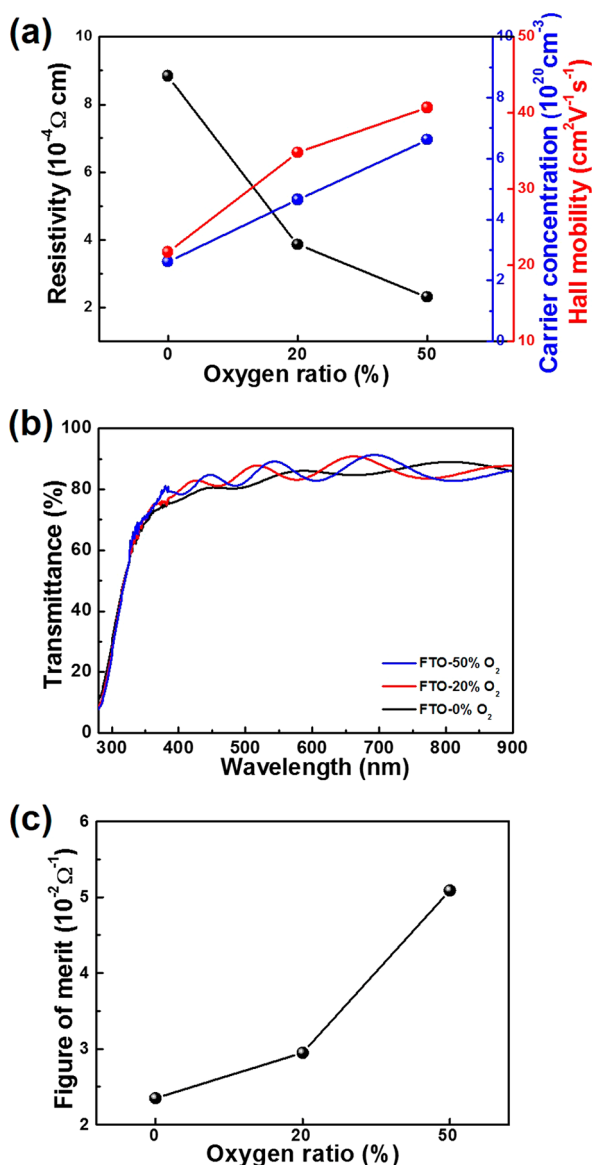
To investigate the chemical binding states and quantity of doping element affecting to electrical properties on the FTO electrodes, the XPS measurements were performed (see Figures 4 and S2). All binding energies were corrected using the C 1s of  $\sim 284.5$  eV as reference. In Figure 4a–c, the XPS Sn 3d<sub>5/2</sub> and Sn 3d<sub>3/2</sub> core-level spectra of all of the electrodes are divided into two characteristic peaks. One is located at  $\sim 486.6$  eV for Sn 3d<sub>5/2</sub> and  $\sim 495.1$  eV Sn 3d<sub>3/2</sub>, corresponding to the binding energy of Sn<sup>4+</sup> in the SnO<sub>2</sub> phase.<sup>35,40</sup> The other is represented at  $\sim 487.7$  eV for Sn 3d<sub>5/2</sub> and  $\sim 496.3$  eV Sn 3d<sub>3/2</sub>, which is assigned to the chemical bond between tin fluorine (Sn–F), indicating the effect of F-substitution in SnO<sub>2</sub> phases.<sup>41,42</sup> This result is also confirmed by XPS F 1s spectra (see Figure S2a–c). In particular, the remarkable difference in the area of the binding energy related to the Sn–F among the FTO electrodes should be noted. Therefore, we determined the surface atomic concentration of O, Sn, and F elements from the corresponding

peak areas in the XPS spectra. As shown in Figure 4d and Table S1, these results suggest that the more O<sub>2</sub> ratio in the carrier gas increases, the more the F-substitution concentration into the SnO<sub>2</sub> is enhanced, which can be induced by the reaction depositing the FTO (see eq 2)).<sup>43</sup>



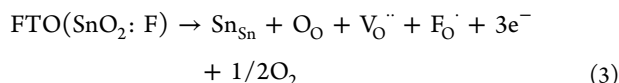
This result may lead to creating free electrons as carriers and making the FTO electrode more conductive.<sup>43,44</sup> As can be seen in Figures S2d–f, the three characteristic peaks from the XPS O 1s core-level spectra were emitted at 530.2, 531.1, and 532.3 eV, indicating the Sn–O, C–OH, and V<sub>O</sub><sup>••</sup>, respectively.<sup>45,46</sup> Interestingly, this result shows that the area ratio of the V<sub>O</sub><sup>••</sup> to Sn–O on the FTO electrodes (0.50 for FTO-0% O<sub>2</sub>, 0.43 for FTO-20% O<sub>2</sub>, and 0.34 for FTO-50% O<sub>2</sub>) gradually decreases with an increase of the O<sub>2</sub> ratio in the carrier gas, which originates from the occupation of oxygen vacancy sites by the increased F-substitution, thereby relaxing the lattice disorder for enhancing Hall mobility on the FTO electrodes.<sup>47</sup> This phenomenon is largely consistent with the FTIR results shown in Figure S3. In the FTIR results, the infrared features observed at 459 and 484 cm<sup>-1</sup> can be assigned to O–Sn–O and F–Sn–F vibrational modes, respectively.<sup>17</sup> Specifically, a gradual enhancement of the infrared feature on O–Sn–O vibrational mode is seen in the FTIR results with the increase of the O<sub>2</sub> ratio in the carrier gas. According to Zhang et al., the weak feature of O–Sn–O vibrational mode corresponds to the existence of V<sub>O</sub><sup>••</sup>, because they deform the O–Sn–O group owing to the compression effect induced by the repulsive force between Sn<sup>4+</sup> and V<sub>O</sub><sup>••</sup>.<sup>17</sup> Based on these results, it can be concluded that the oxygen activation can lead to a decline in the V<sub>O</sub><sup>••</sup> instead of increasing the F<sub>O</sub><sup>•</sup>, as shown in the XPS results. Therefore, the change in the V<sub>O</sub><sup>••</sup> and F<sub>O</sub><sup>•</sup> induced by the oxygen activation can affect the carrier concentration and Hall mobility in the FTO electrodes.

Figure 5a shows the electrical properties of the FTO electrodes with various O<sub>2</sub> ratios in the carrier gas, including the



**Figure 5.** (a) Electrical properties, (b) optical transmittance spectra in the visible range, and (c) FOM as a function of the  $\text{O}_2$  ratio (0, 20, and 50%).

carrier concentration, Hall mobility, and resistivity. The carrier concentration gradually enhances from  $\sim 2.60 \times 10^{20}$  to  $\sim 6.62 \times 10^{20} \text{ cm}^{-3}$ , when the  $\text{O}_2$  ratio increases from 0% to 50%. This behavior of the carrier concentration can be explained through the defect mechanism of the FTO structure (see eq 3).



According to eq 3, the carrier concentration of FTO can be influenced by the presence of  $\text{V}_{\text{O}}^{\bullet\bullet}$  and  $\text{F}_{\text{O}}^{\bullet}$  in the FTO structure. However, the oxygen activation on the FTO electrodes (FTO-50%  $\text{O}_2$ ) can cause the decline of the  $\text{V}_{\text{O}}^{\bullet\bullet}$  as follows (see eq 4),<sup>48</sup> which was also proved by the XPS (Figure S2) and FTIR results (Figure S3).



Therefore, improving their carrier concentration should be due to the effect of the increased  $\text{F}_{\text{O}}^{\bullet}$  concentration induced by the

oxygen activation, thus resulting in the high carrier concentration (see Table 1).<sup>26,44</sup> In addition, for Hall mobilities, an

**Table 1.** Summary of Electrical and Optical Properties Obtained from All of the Electrodes

	FTO-0% $\text{O}_2$	FTO-20% $\text{O}_2$	FTO-50% $\text{O}_2$
carrier concentration ( $\text{cm}^{-3}$ )	$2.60 \times 10^{20}$	$4.65 \times 10^{20}$	$6.62 \times 10^{20}$
Hall mobility ( $\text{cm}^2/(\text{V s})$ )	27.1	34.8	40.7
resistivity ( $\Omega \text{ cm}$ )	$8.84 \times 10^{-4}$	$3.85 \times 10^{-4}$	$2.31 \times 10^{-4}$
sheet resistance ( $\Omega/\square$ )	$15.8 \pm 0.65$	$7.0 \pm 0.31$	$4.0 \pm 0.14$
transmittance (%)	83.9	85.1	85.3

increased value from  $\sim 27.1 \text{ cm}^2/(\text{V s})$  for FTO-0%  $\text{O}_2$  to  $\sim 40.7 \text{ cm}^2/(\text{V s})$  for FTO-50%  $\text{O}_2$  is observed, which is consistent with the dominant growth of (200) preferred orientations and the relaxation of the FTO lattice disorder by the decreased  $\text{V}_{\text{O}}^{\bullet\bullet}$ . According to Agashe et al., the (200) preferred orientations in the FTO electrode offer a compact structure for the growing films.<sup>26,38</sup> The SEM results (Figures 3c,f) demonstrate that the use of carrier gas with the ratio of 50%  $\text{O}_2$  leads to the formation of the uniform FTO electrodes by the dominant growth of (200) preferred orientations, which can assist the enhancement of Hall mobility by reducing the carrier scattering at the grain boundaries and surface.<sup>22,31</sup> In addition, Hall mobility is directly related to the lattice distortion on the FTO electrodes. That is, the reduction of the  $\text{V}_{\text{O}}^{\bullet\bullet}$  induced by oxygen activation can lead to the distortion relaxation on the FTO lattices, which is proved by the decreased Urbach energy ( $\alpha = \alpha_0 \exp(h\nu/E_u)$ , where  $\alpha$  is absorption coefficient,  $h\nu$  is photon energy, and  $E_u$  is Urbach energy with increase of the  $\text{O}_2$  ratio (see Figure S4), causing an increase of Hall mobility resulting from the decrease in the ionized impurity scattering.<sup>47</sup> Therefore, based on the carrier concentration ( $N$ ) and Hall mobility ( $\mu$ ), the resistivity ( $\rho$ ) of the FTO electrodes can be obtained using the following relationship (see eq 5):<sup>49</sup>

$$\rho = 1/(Ne\mu) \quad (5)$$

where  $e$  is the electron charge ( $1.602 \times 10^{-19} \text{ C}$ ). Therefore, the resistivity values ( $\rho$ ) were obtained to be  $\sim 8.84 \times 10^{-4} \Omega \text{ cm}$  for FTO-0%  $\text{O}_2$ ,  $\sim 3.85 \times 10^{-4} \Omega \text{ cm}$  for FTO-20%  $\text{O}_2$ , and  $\sim 2.31 \times 10^{-4} \Omega \text{ cm}$  for FTO-50%  $\text{O}_2$ . In addition, the sheet resistances calculated by the resistivity/thickness of the FTO electrodes were  $\sim 15.8 \pm 0.65 \Omega/\square$  for FTO-0%  $\text{O}_2$ ,  $\sim 7.0 \pm 0.31 \Omega/\square$  for FTO-20%  $\text{O}_2$ , and  $\sim 4.0 \pm 0.14 \Omega/\square$  for FTO-50%  $\text{O}_2$ , indicating that FTO-50%  $\text{O}_2$  have excellent electrical properties as compared to others. This performance improvement is attributed to the main effects of the oxygen activation on the FTO electrodes (see Figure 6): the increased carrier concentration by the enhanced  $\text{F}_{\text{O}}^{\bullet}$  concentration and the enhanced Hall mobility originates from formation of uniform FTO electrode with (200) preferred orientations and distortion relaxation on the FTO lattice. Figure 5b shows the optical transmittances of the FTO electrodes. The spectra show that the FTO electrodes have the average optical transmittance of  $\sim 83.9\%$  for FTO-0%  $\text{O}_2$ ,  $\sim 85.1\%$  for FTO-20%  $\text{O}_2$ , and  $\sim 85.3\%$  for FTO-50%  $\text{O}_2$  in the wavelength range of 400–800 nm. This suggests that the minute increase in the optical transmittance of the electrodes is generated when the  $\text{O}_2$  ratio of carrier gas varies from 0% to 50%, which is due to the reduced reflection of the light by less textured surface (uniform surface morphology), thus causing the good transparency on

## Effect of oxygen activation on FTO electrodes

→ outstanding transparent conducting performances

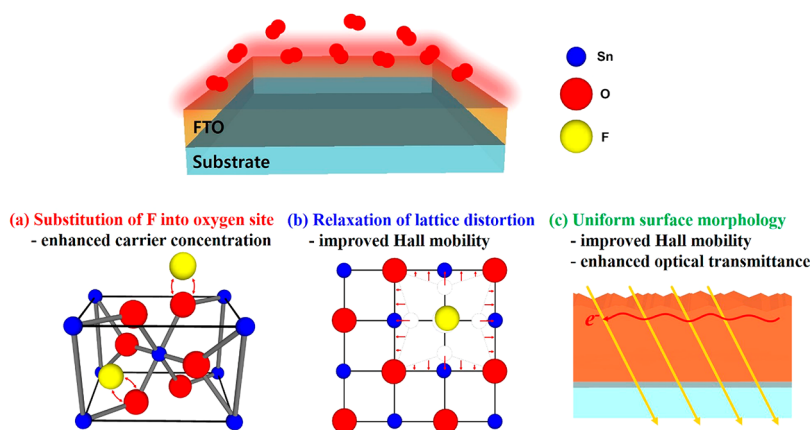


Figure 6. Schematic illustration of the oxygen activation on FTO electrodes with main effects to improve transparent conducting performances.

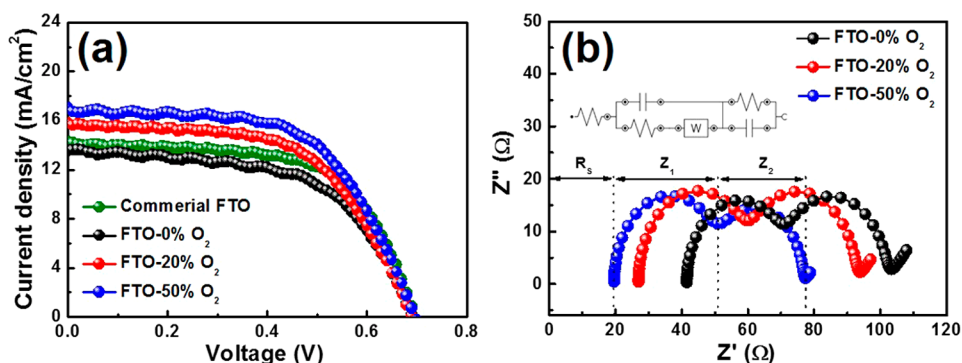


Figure 7. (a) Photocurrent–voltage ( $J$ – $V$ ) curves and (b) Nyquist plot of the EIS obtained from the DSSCs assembled with the prepared FTO electrodes for working and counter electrodes.

Table 2. Photovoltaic Performances and EIS Elements for the DSSCs Assembled with the FTO Electrodes

	$V_{OC}$ (V)	$J_{SC}$ (mA/cm <sup>2</sup> )	ff (%)	$\eta$ (%)	$R_s$ (Ω)	$Z_1$ (Ω)	$Z_2$ (Ω)
commercial FTO (8.0 Ω/□)	0.69 ± 0.01	15.9 ± 0.52	57.7 ± 0.02	6.37 ± 0.26			
FTO-0% O <sub>2</sub>	0.69 ± 0.01	13.6 ± 0.41	57.6 ± 0.01	5.40 ± 0.24	41.5	29.4	30.7
FTO-20% O <sub>2</sub>	0.69 ± 0.01	15.8 ± 0.46	58.0 ± 0.03	6.33 ± 0.22	26.9	33.0	32.5
FTO-50% O <sub>2</sub>	0.69 ± 0.01	17.0 ± 0.50	59.2 ± 0.02	7.03 ± 0.20	19.5	31.3	25.9

the FTO electrode formed at 50% O<sub>2</sub><sup>50</sup> (see Figure 6). In addition, we determined the optical band gap of all of the electrodes from optical transmittance spectra (see Figure S5). The optical band gap is based on the relation between the absorption coefficient ( $\alpha$ ) and the incident photo energy ( $h\nu$ ; see eq 6):<sup>51</sup>

$$(\alpha h\nu)^2 = D(h\nu - E_g)^n \quad (6)$$

where  $h\nu$ ,  $D$ , and  $E_g$  are the photon energy, optical band gap, and constant, respectively. Their optical band gaps are calculated to be  $\sim 4.14$  eV for FTO-0% O<sub>2</sub>,  $\sim 4.09$  eV for FTO-20% O<sub>2</sub>, and  $\sim 4.04$  eV for FTO-50% O<sub>2</sub>. These results indicate that a decrease in the optical band gap can be induced by an increased O<sub>2</sub> ratio in the carrier gas, which is due to the enhanced F<sub>O</sub><sup>•</sup> concentration by the oxygen activation. That is, F doping in SnO<sub>2</sub> causes the formation of the Fermi level to enter the conduction band and then the degeneracy of the energy levels by the interaction between F 2p states and the Sn 2s and Sn 2p states, resulting in the band gap narrowing and

increased carrier concentration on the FTO electrodes.<sup>51,52</sup> Furthermore, based on their electrical and optical properties summarized in Table 1, a figure of merit (FOM,  $\phi$ ) is calculated to predict the performance as a TCE, which is defined as  $\phi = T^{10}/R_{sh}$ , where  $T$  is the optical transmittance in the visible range and  $R_{sh}$  is the sheet resistance.<sup>25</sup> As shown in Figure S5c, FTO-50% O<sub>2</sub> have the highest FOM value ( $\sim 5.09 \pm 0.19 \times 10^{-2} \Omega^{-1}$ ) compared to others. Specifically, these electrical properties are comparable to the previous results related to high-performance FTO electrodes fabricated using various processes (see Table S2).<sup>19–23,26,53,54</sup> As such, FTO-50% O<sub>2</sub> show the best transparent conducting performance owing to their excellent sheet resistance ( $\sim 4.0 \pm 0.14 \Omega/\square$ ) and optical transmittance ( $\sim 85.3\%$ ) as result of oxygen activation.

Figure 7a shows the photocurrent–voltage ( $J$ – $V$ ) curves of DSSCs with the prepared FTO electrodes as the current collector for both working and counter electrodes. The photoconversion efficiency (PCE,  $\eta$ ) of DSSCs can be obtained from the following relationship (see eq 7):<sup>55</sup>

$$\eta(\%) = (J_{sc} V_{oc} ff) / (I_{max} V_{max}) \quad (7)$$

where  $J_{sc}$ ,  $V_{oc}$ ,  $ff$ ,  $I_{max}$ , and  $V_{max}$  are the short-circuit current density, open-circuit voltage, fill factor, maximum power current, and maximum power voltage, respectively. The obtained photovoltaic parameters of each cell are summarized in Table 2. The  $V_{oc}$  is determined by the difference of electrical potential between two electrodes composed of the DSSCs. Therefore, the retained  $V_{oc}$  among the cells is observed because all DSSCs are composed of the same components with  $\text{TiO}_2$  as the working electrode and Pt as the counter electrode.<sup>56</sup> Furthermore, while the  $ff$  values among the cells are similar due to the same composition, including the FTO electrode,  $\text{TiO}_2$ , Pt, and electrolyte,<sup>1,16</sup> it should be noted that, with an increase of the  $\text{O}_2$  ratio in the carrier gas, the  $J_{sc}$  value increased from  $13.6 \pm 0.41 \text{ mA/cm}^2$  at FTO-0%  $\text{O}_2$  to  $15.8 \pm 0.46 \text{ mA/cm}^2$  at FTO-20%  $\text{O}_2$  and  $17.0 \pm 0.50 \text{ mA/cm}^2$  at FTO-50%  $\text{O}_2$ . Therefore, the DSSCs with FTO-50%  $\text{O}_2$  generate the best PCE of  $\sim 7.03 \pm 0.20\%$ , with  $V_{oc}$  of  $0.69 \pm 0.01 \text{ V}$  and  $ff$  of  $59.2 \pm 0.02\%$ . In the DSSC, the photovoltaic performances are related to the sheet resistance and light absorbance of TCE.<sup>22,55,57</sup> Therefore, this performance improvement may be mainly due to the dominant effect of the decreased sheet resistance of FTO used as the TCEs, although they exhibited good optical transmittance in the UV-vis result (see Figure 5b). Therefore, in order to determine the main factor of the FTO electrodes for improving the photovoltaic performance, we measured the internal resistances in DSSCs using electrochemical impedance spectroscopy (EIS). Figure 7b shows the measured Nyquist plots of DSSCs using the FTO electrodes, where the plots are divided into three characteristic parts related to the sheet resistance in the FTO electrode ( $R_s$ , series resistance), charge transfer at the interface between the counter electrode/electrolyte ( $Z_1$ ), and  $\text{TiO}_2/\text{dye}/\text{electrolyte}$  ( $Z_2$ ).<sup>58,59</sup> The EIS elements obtained from the fitted Nyquist plots are summarized in Table 2. As expected, the  $R_s$  of FTO-50%  $\text{O}_2$  represents the lowest value ( $19.5 \Omega$ ) as compared to other electrodes, corresponding to the results of the sheet resistance in Figure 5a, whereas other two values ( $Z_1$  and  $Z_2$ ) are identical. Furthermore, in order to further confirm the effect of the optical transmittance on the photovoltaic performance of DSSCs, we investigated the absorption spectra of the half cells with the working electrodes containing the dye (see Figure S6). It is noted that the absorption in the range of 400–800 nm has similar values among the electrodes. Therefore, the photovoltaic performance improvement of the DSSC with FTO-50%  $\text{O}_2$  is directly related to the decreased sheet resistance resulting from the synergistic effect of the enhanced carrier concentration by high F-doping concentration and the fasted Hall mobility by a uniform surface morphology and relaxation of the FTO lattice distortion. These results indicate that the highly transparent conducting FTO electrodes fabricated using the oxygen activation of HUSPD can reasonably be expected to be attractive TCEs for the DSSCs.

## CONCLUSIONS

In the present study, we fabricated highly transparent conducting FTO electrodes with the help of the oxygen activation of the HUSPD by adjusting the  $\text{O}_2$  ratio in the carrier gas (0%, 20%, and 50%). Compared to the normal SPD, the HUSPD where the precursor droplets are horizontally supplied to the substrates is an attractive technique to form uniform film nanostructures due to the uniformly distributed gas flow. As a

result, compared to other electrodes, the FTO electrodes fabricated at 50%  $\text{O}_2$  have excellent sheet resistance ( $\sim 4.0 \pm 0.14 \Omega/\square$ ), optical transmittance ( $\sim 85.3\%$ ), and FOM ( $\sim 5.09 \pm 0.19 \times 10^{-2} \Omega^{-1}$ ), which can be attributed to the improved  $F_{O_2}$  concentration relative to the supply of the high carrier concentration and the formation of a uniform surface structure and relaxation of the FTO lattice distortion relative to efficient Hall mobility and relaxation of the light scattering at the electrodes. In addition, the DSSC fabricated with this electrode exhibited a high photoconversion efficiency ( $\sim 7.03 \pm 0.20\%$ ) by the improved  $J_{sc}$  value. The main factor of the photovoltaic performance improvement is due to the decreased sheet resistance of the FTO used as TCE, which is caused by the simultaneous improvement of their carrier concentration and Hall mobility. Therefore, we assume that the FTO electrodes fabricated using the oxygen activation of HUSPD have an excellent potential for further use as attractive TCEs for various optoelectronic applications such as DSSCs.

## ASSOCIATED CONTENT

### Supporting Information

The Supporting Information is available free of charge on the ACS Publications website at DOI: 10.1021/acsami.7b12968.

Additional materials including tables and figures as discussed in the text. (PDF)

## AUTHOR INFORMATION

### Corresponding Authors

\*E-mail: dhriu15@seoultech.ac.kr.

\*E-mail: hjahn@seoultech.ac.kr.

### ORCID

Hyo-Jin Ahn: 0000-0002-5786-3937

### Notes

The authors declare no competing financial interest.

## ACKNOWLEDGMENTS

This work was supported by Grant No. 10041161 from the Ministry of Knowledge Economy (MKE) and the Fundamental R&D Program for Core Technology of Materials funded by the Ministry of Knowledge Economy, Republic of Korea.

## REFERENCES

- (1) Tsai, C.-H.; Hsu, S.-Y.; Huang, T.-W.; Tsai, Y.-T.; Chen, Y.-F.; Jhang, Y. H.; Hsieh, L.; Wu, C.-C.; Chen, Y.-S.; Chen, C.-W.; Li, C.-C. Influences of Textures in Fluorine-doped Tin Oxide on Characteristics of Dye-sensitized Solar Cells. *Org. Electron.* **2011**, *12*, 2003–2011.
- (2) Brisse, R.; Faddoul, R.; Bourgeteau, T.; Tondelier, D.; Leroy, J.; Campidelli, S.; Berthelot, T.; Geffroy, B.; Jusselme, B. Inkjet Printing NiO-Based p-Type Dye-Sensitized Solar Cells. *ACS Appl. Mater. Interfaces* **2017**, *9*, 2369–2377.
- (3) Kwon, J.; Park, N.-G.; Lee, J. Y.; Ko, M.-J.; Park, J. H. Highly Efficient Monolithic Dye-Sensitized Solar Cells. *ACS Appl. Mater. Interfaces* **2013**, *5*, 2070–2074.
- (4) Bessho, T.; Zakeeruddin, S. M.; Yeh, C.-Y.; Diau, E. W.-G.; Grätzel, M. Highly Efficient Mesoscopic Dye-Sensitized Solar Cells Based on Donor-Acceptor-Substituted Porphyrins. *Angew. Chem.* **2010**, *122*, 6796–6799.
- (5) Grätzel, M. Photoelectrochemical Cells. *Nature* **2001**, *414*, 338–344.
- (6) Kim, B.-M.; Han, H.-G.; Kim, J. S.; Shin, H.; Kwon, T.-H. Control and Monitoring of Dye Distribution in Mesoporous  $\text{TiO}_2$

Film for Improving Photovoltaic Performance. *ACS Appl. Mater. Interfaces* **2017**, *9*, 2572–2580.

(7) Huang, F.; Chen, D.; Cao, L.; Caruso, R. A.; Cheng, Y.-B. Flexible Dye-sensitized Solar Cells Containing Multiple Dyes in Discrete Layers. *Energy Environ. Sci.* **2011**, *4*, 2803–2806.

(8) Qian, X.; Li, H.; Shao, L.; Jiang, X.; Hou, L. Morphology-Tuned Synthesis of Nickel Cobalt Selenides as Highly Efficient Pt-Free Counter Electrode Catalysts for Dye-Sensitized Solar Cells. *ACS Appl. Mater. Interfaces* **2016**, *8*, 29486–29495.

(9) Im, H.-G.; An, B. W.; Jin, J.; Jang, J.; Park, Y.-G.; Park, J.-U.; Bae, B.-S. A High-performance, Flexible and Robust Metal Nanotrough-embedded Transparent Conducting Film for Wearable Touch Screen Panels. *Nanoscale* **2016**, *8*, 3916–3922.

(10) Baetens, R.; Jelle, B. P.; Gustavsen, A. Properties, Requirements and Possibilities of Smart Windows for Dynamic Daylight and Solar Energy Control in Buildings: A State-of-the-art Review. *Sol. Energy Mater. Sol. Cells* **2010**, *94*, 87–105.

(11) Yang, Y.; Huang, Q.; Metz, A. W.; Ni, J.; Jin, S.; Marks, T. J.; Madsen, M. E.; DiVenere, A.; Ho, S.-T. High-Performance Organic Light-Emitting Diodes Using ITO Anodes Grown on Plastic by Room-Temperature Ion-Assisted Deposition. *Adv. Mater.* **2004**, *16*, 321–324.

(12) Lee, J.; Jung, B.-J.; Lee, J.-I.; Chu, H. Y.; Do, L.-M.; Shim, H.-K. Modification of an ITO Anode with a Hole-transporting SAM for Improved OLED Device Characteristics. *J. Mater. Chem.* **2002**, *12*, 3494–3498.

(13) Chantarat, N.; Hsu, S.-H.; Lin, C.-C.; Chiang, M.-C.; Chen, S.-Y. Mechanism of an AZO-coated FTO film in Improving the Hydrogen Plasma Durability of Transparent Conducting Oxide Thin Films for Amorphous-silicon based Tandem Solar Cells. *J. Mater. Chem.* **2012**, *22*, 8005–8012.

(14) Kim, C.-Y.; Riu, D.-H. Texture Control of Fluorine-doped Tin Oxide Thin Film. *Thin Solid Films* **2011**, *519*, 3081–3085.

(15) Noh, S. I.; Ahn, H.-J.; Riu, D.-H. Photovoltaic Property Dependence of Dye-sensitized Solar Cells on Sheet Resistance of FTO Substrate deposited via Spray Pyrolysis. *Ceram. Int.* **2012**, *38*, 3735–3739.

(16) Bae, J.-W.; Koo, B.-R.; An, H.-R.; Ahn, H.-J. Surface Modification of Fluorine-doped Tin Oxide Films using Electrochemical Etching for Dye-sensitized Solar Cells. *Ceram. Int.* **2015**, *41*, 14668–14673.

(17) Zhang, B.; Tian, Y.; Zhang, J. X.; Cai, W. The Role of Oxygen Vacancy in Fluorine-doped SnO<sub>2</sub> Films. *Phys. B* **2011**, *406*, 1822–1826.

(18) Kilic, C.; Zunger, A. Origins of Coexistence of Conductivity and Transparency in SnO<sub>2</sub>. *Phys. Rev. Lett.* **2002**, *88*, 095501.

(19) Maruyama, T.; Akagi, H. Fluorine-Doped Tin Dioxide Thin Films Prepared by Radio-Frequency Magnetron Sputtering. *J. Electrochem. Soc.* **1996**, *143*, 283–287.

(20) Noor, N.; Parkin, I. P. Enhanced Transparent-conducting Fluorine-doped Tin Oxide Films formed by Aerosol-Assisted Chemical Vapour Deposition. *J. Mater. Chem. C* **2013**, *1*, 984–996.

(21) Kim, H.; Auyeung, R. C. Y.; Piqué, A. Transparent conducting F-doped SnO<sub>2</sub> Thin Films by pulsed laser deposition. *Thin Solid Films* **2008**, *516*, 5052–5056.

(22) Nadarajah, A.; Carnes, M. E.; Kast, M. G.; Johnson, D. W.; Boettcher, S. W. Aqueous Solution Processing of F-Doped SnO<sub>2</sub> Transparent Conducting Oxide Films Using a Reactive Tin(II) Hydroxide Nitrate Nanoscale Cluster. *Chem. Mater.* **2013**, *25*, 4080–4087.

(23) Fukano, T.; Motohiro, T. Low-temperature Growth of Highly Crystallized Transparent Conductive Fluorine-doped Tin Oxide Films by Intermittent Spray Pyrolysis Deposition. *Sol. Energy Mater. Sol. Cells* **2004**, *82*, 567–575.

(24) Aparicio, M.; Jitianu, A.; Klein, L. C. *Sol-gel processing for conventional and alternative energy*; Springer: Berlin, Germany, 2012.

(25) Jeon, B. J.; Hudaya, C.; Lee, J. K. Pilot-scale Electron Cyclotron Resonance-metal Organic Chemical Vapor Deposition System for the Preparation of Large-area Fluorine-doped SnO<sub>2</sub> Thin Films. *J. Vac. Sci. Technol., A* **2016**, *34*, 031501.

(26) Agashe, C.; Hüpkens, J.; Schöpe, G.; Berginski, M. Physical Properties of Highly Oriented Spray-deposited Fluorine-doped Tin Dioxide Films as Transparent Conductor. *Sol. Energy Mater. Sol. Cells* **2009**, *93*, 1256–1262.

(27) Benhaoua, A.; Rahal, A.; Benhaoua, B.; Jlassi, M. Effect of Fluorine Doping on the Structural, Optical and Electrical Properties of SnO<sub>2</sub> Thin Films prepared by Spray Ultrasonic. *Superlattices Microstruct.* **2014**, *70*, 61–69.

(28) Otsuka, R.; Endo, T.; Takano, T.; Takemura, S.; Murakami, R.; Muramoto, R.; Madarász, J.; Okuya, M. Fluorine Doped Tin Oxide Film with High Haze and Transmittance Prepared for Dye-sensitized Solar Cells. *Jpn. J. Appl. Phys.* **2015**, *54*, 08KF03.

(29) Schubert, U.; Hüsing, N. *Synthesis of inorganic materials*, 3rd ed.; Wiley-VCH: Weinheim, Germany, 2000.

(30) Farrow, R. F. C.; Parkin, S. S. P.; Dobson, P. J.; Neave, J. H.; Arrott, A. S. *Thin film growth techniques for low-dimensional structures*; Plenum: New York, 1987.

(31) Wang, H.; Fu, F.; Zhang, F.; Wang, H.-E.; Kershaw, S. V.; Xu, J.; Sun, S.-G.; Rogach, A. L. Hydrothermal Synthesis of Hierarchical SnO<sub>2</sub> Microspheres for Gas Sensing and Lithium-ion Batteries Applications: Fluoride-Mediated Formation of Solid and Hollow Structures. *J. Mater. Chem.* **2012**, *22*, 2140–2148.

(32) Moholkar, A. V.; Pawar, S. M.; Rajpure, K. Y.; Bhosale, C. H.; Kim, J. H. Effect of Fluorine Doping on Highly Transparent Conductive Spray Deposited Nanocrystalline Tin Oxide Thin Films. *Appl. Surf. Sci.* **2009**, *255*, 9358–9364.

(33) Smith, A.; Laurent, J.-M.; Smith, D. S.; Bonnet, J.-P.; Clemente, R. R. Relation between Solution Chemistry and Morphology of SnO<sub>2</sub>-based Thin Films deposited by a Pyrosol Process. *Thin Solid Films* **1995**, *266*, 20–30.

(34) Korotkov, R. Y.; Ricou, P.; Farran, A. J. E. Preferred Orientations in Polycrystalline SnO<sub>2</sub> Films grown by Atmospheric Pressure Chemical Vapor Deposition. *Thin Solid Films* **2006**, *502*, 79–87.

(35) Murakami, K.; Yagi, I.; Kaneko, S. Oriented Growth of Tin Oxide Thin Films on Glass Substrates by Spray Pyrolysis of Organotin Compounds. *J. Am. Ceram. Soc.* **1996**, *79*, 2557–2562.

(36) Volintiru, I.; Creatore, M.; Kniknie, B. J.; Spee, C. I. M. A.; van de Sanden, M. C. M. Evolution of the Electrical and Structural Properties during the Growth of Al doped ZnO Films by Remote Plasma-enhanced Metalorganic Chemical Vapor Deposition. *J. Appl. Phys.* **2007**, *102*, 043709.

(37) Frey, H.; Khan, H. R. *Handbook of thin-film technology*; Springer: Berlin, Germany, 2015.

(38) Omura, K.; Veluchamy, P.; Tsuji, M.; Nishio, T.; Murozono, M. A Pyrosol Technique to Deposit Highly Transparent, Low-Resistance SnO<sub>2</sub>:F Thin Films from Dimethyltin Dichloride. *J. Electrochem. Soc.* **1999**, *146*, 2113–2116.

(39) Cho, C.-W.; Lee, J.-H.; Riu, D.-H.; Kim, C.-Y. Fast Responsive Gas Sensor of Vertically Aligned Fluorine-Doped Tin Oxide Nanorod Thin Film. *Jpn. J. Appl. Phys.* **2012**, *51*, 04S001.

(40) Wang, Y. D.; Djerdj, I.; Antoniotti, M.; Smarsly, B. Polymer-Assisted Generation of Antimony-Doped SnO<sub>2</sub> Nanoparticles with High Crystallinity for Application in Gas Sensors. *Small* **2008**, *4*, 1656–1660.

(41) Jung, H.-G.; Yoon, C. S.; Prakash, J.; Sun, Y.-K. Mesoporous Anatase TiO<sub>2</sub> with High Surface Area and Controllable Pore Size by F<sup>-</sup>-Ion Doping: Applications for High-Power Li-Ion Battery Anode. *J. Phys. Chem. C* **2009**, *113*, 21258–21263.

(42) Park, J. H.; Jang, S.; Byun, D.; Lee, J. K. Fluorine Doped Gallium Tin Oxide Composite Films as Transparent Conductive Oxides on Polyethylene Terephthalate Film prepared by Electron Cyclotron Resonance Metal Organic Chemical Vapor Deposition. *Thin Solid Films* **2011**, *519*, 6863–6867.

(43) Ma, H. L.; Zhang, D. H.; Chen, Y. P.; Li, S. Y.; Ma, J.; Zong, F. J. Large Scale Fluorine Doped Textured Transparent Conducting SnO<sub>2</sub> Films deposited by Atmospheric Pressure Chemical Vapor Deposition. *Thin Solid Films* **1997**, *298*, 151–155.

- (44) Kumar, V.; Govind, A.; Nagarajan, R. Optical and Photocatalytic Properties of Heavily F<sup>-</sup>-Doped SnO<sub>2</sub> Nanocrystals by a Novel Single-Source Precursor Approach. *Inorg. Chem.* **2011**, *50*, 5637–5645.
- (45) Choi, M.-S.; Lee, Y.-J.; Kwon, J.-D.; Jeong, Y.; Park, J.-Y.; Kang, Y.-C.; Song, P.-K.; Kim, D.-H. Effects of Hydrogen Plasma Treatment on SnO<sub>2</sub>:F Substrates for Amorphous Si Thin Film Solar Cells. *Curr. Appl. Phys.* **2013**, *13*, 1589–1593.
- (46) Seo, H.-K.; Song, M.; Ameen, S.; Akhtar, M. S.; Shin, H. S. New Counter Electrode of Hot Filament Chemical Vapor deposited Graphene Thin Film for Dye Sensitized Solar Cell. *Chem. Eng. J.* **2013**, *222*, 464–471.
- (47) Agashe, C.; Major, S. S. Effect of Heavy Doping in SnO<sub>2</sub>:F Films. *J. Mater. Sci.* **1996**, *31*, 2965–2969.
- (48) Kizaki, Y.; Noguchi, Y.; Miyayama, M. Defect Control for Low Leakage Current in K<sub>0.5</sub>Na<sub>0.5</sub>Nb O<sub>3</sub> single crystals. *Appl. Phys. Lett.* **2006**, *89*, 142910.
- (49) van der Pauw, L. J. A Method of Measuring Specific Resistivity and Hall Effect of Discs of Arbitrary Shape. *Philips Res. Repts.* **1958**, *13*, 1–9.
- (50) Jäger, K.; Zeman, M. A Scattering Model for Surface-textured Thin Films. *Appl. Phys. Lett.* **2009**, *95*, 171108.
- (51) Ghosh, P. K.; Das, S.; Kundoo, S.; Chattopadhyay, K. K. Effect of Fluorine Doping on Semiconductor to Metal-Like Transition and Optical Properties of Cadmium Oxide Thin Films Deposited by Sol-Gel Process. *J. Sol-Gel Sci. Technol.* **2005**, *34*, 173–179.
- (52) Xu, J.; Huang, S.; Wang, Z. First Principle Study on the Electronic Structure of Fluorine-doped SnO<sub>2</sub>. *Solid State Commun.* **2009**, *149*, 527–531.
- (53) Lin, C.-C.; Chiang, M.-C.; Chen, Y.-W. Temperature Dependence of Fluorine-doped Tin Oxide Films produced by Ultrasonic Spray Pyrolysis. *Thin Solid Films* **2009**, *518*, 1241–1244.
- (54) Martinez, A. I.; Acosta, D. R. Effect of the fluorine content on the structural and electrical properties of SnO<sub>2</sub> and ZnO-SnO<sub>2</sub> thin films prepared by spray pyrolysis. *Thin Solid Films* **2005**, *483*, 107–113.
- (55) Grätzel, M. Dye-sensitized Solar Cells. *J. Photochem. Photobiol., C* **2003**, *4*, 145–153.
- (56) Koo, B.-R.; An, H.; Ahn, H.-J. High-surface Area Co-electrospun TiO<sub>2</sub> Nanowires Fabricated using Shrinkage of Polyvinylpyrrolidone for Improved Photovoltaic Performance. *Ceram. Int.* **2016**, *42*, 1666–1671.
- (57) Hore, S.; Vetter, C.; Kern, R.; Smit, H.; Hinsch, A. Influence of Scattering Layers on Efficiency of Dye-sensitized Solar Cells. *Sol. Energy Mater. Sol. Cells* **2006**, *90*, 1176–1188.
- (58) Wang, F.; Subbaiyan, N. K.; Wang, Q.; Rochford, C.; Xu, G.; Lu, R.; Elliot, A.; D'Souza, F.; Hui, R.; Wu, J. Development of Nanopatterned Fluorine-Doped Tin Oxide Electrodes for Dye-Sensitized Solar Cells with Improved Light Trapping. *ACS Appl. Mater. Interfaces* **2012**, *4*, 1565–1572.
- (59) Lin, L.-Y.; Tsai, C.-H.; Wong, K.-T.; Huang, T.-W.; Hsieh, L.; Liu, S.-H.; Lin, H.-W.; Wu, C.-C.; Chou, S.-H.; Chen, S.-H.; Tsai, A.-I. Organic Dyes Containing Coplanar Diphenyl-Substituted Dithienosilole Core for Efficient Dye-Sensitized Solar Cells. *J. Org. Chem.* **2010**, *75*, 4778–4785.